Cross-stream migration of drops suspended in Poiseuille flow in the presence of an electric field

Binita Nath,[1] Gautam Biswas,[1,*] Amaresh Dalal,[1] and Kirti Chandra Sahu[2]
[1]*Department of Mechanical Engineering, Indian Institute of Technology Guwahati, Guwahati 781039, India*
[2]*Department of Chemical Engineering, Indian Institute of Technology Hyderabad, Sangareddy 502 285, Telangana, India*

(Received 10 February 2018; revised manuscript received 30 April 2018; published 18 June 2018)

The present study focuses on the cross-stream migration of a neutrally buoyant two-dimensional drop in a Poiseuille flow in a channel under the influence of an electric field. In the absence of an electric field, the important nondimensional parameters describing this problem are the viscosity ratio (λ) between the drop fluid and the surrounding medium, the ratio of drop diameter to channel height (a^*), and the capillary number (Ca). The influence of all these parameters on drop migration is investigated. It is observed that a large drop moves slowly as compared to a smaller drop, but attains a steady shape at the center line of the channel. The increase in value of the capillary number enhances the cross-stream migration rate, while the increase in viscosity ratio reduces the tendency of the drops to move towards the channel center line. The presence of an electric field introduces additional interfacial stresses at the drop interface, which in turn alters the dynamics observed in the absence of an electric field. Extensive computations are carried out to analyze the combined effect of the electric field and the shear flow on the cross-stream migration of the drop. The computational results for a perfect dielectric indicate that the droplet migration enhances in the presence of an electric field. The permittivity ratio (S) and the electric field strength (E) play major roles in drop migration and deformation. Computations using the leaky dielectric model also show that for certain combinations of electrical properties the drop undergoes immense elongation along the direction of the electric field. The conductivity ratio (R) is again a vital parameter in such a system of fluids. It is further observed that for certain conditions the leaky dielectric drops exhibit rotation together with translation.

DOI: 10.1103/PhysRevE.97.063106

I. INTRODUCTION

The motion of a liquid drop suspended in Poiseuille flow in another immiscible medium inside a microchannel is a fundamental problem that stands very important from physical, biological, and engineering viewpoints. The droplet motion and deformation in microchannels and capillary tubes has been studied by researchers for decades. The dynamics of a droplet in hydrodynamics flows through channel or tube has been experimentally studied by Goldsmith and Mason [1], Olbritch [2], Ho and Leal [3], and Olbrtich and Kung [4], at low Reynolds number. Ho and Leal [3] investigated the effects of capillary number and viscosity ratio on droplet shapes. Olbricht and Kung [4] studied experimentally the motion of drops in a capillary tube for a large range of capillary numbers, drop sizes, and viscosity ratios. They reported the effects of drop size and viscosity ratio on the critical capillary number above which the drop breakup occurs. In the Stokes flow limit, Chan and Leal [5] and Nadim and Stone [6] investigated the effects of the viscosity ratio and the capillary number Ca on the migration of droplets with diameter much smaller that channel height. In addition to the experimental and theoretical studies, most of the numerical investigations for simulating the behavior of a single gas bubble or drop in Poiseuille flow at zero Reynolds number (Stokes flow approximation) were carried out using the boundary-integral method [7–12]. On the other hand, Mortazavi and Tryggvason [13] studied the deformation and lateral migration of a two-dimensional (2D) drop in a flow channel at finite Reynolds number using the full Navier-Stokes equations with a finite-difference and front-tracking approach. Konda *et al.* [14] numerically studied migration of a droplet in a converging-diverging channel using a finite-volume approach and demonstrated droplet shape oscillations while it migrates inside the channel due to an imposed pressure gradient. Nourbaksh and Mortazavi [15] reported the dependency of the drop migration on the viscosity ratio. Recently Nath *et al.* [16] studied the droplet motion in capillary tubes adopting a coupled-level-set-volume-of-fluid approach [17] and discussed the dynamics associated with droplet breakup.

Several theoretical, numerical, and experimental studies have also been carried out that explore the effects of application of an electric field to various fluid systems. The pioneering theoretical works of O'Konski and Thatcher [18] and Garton and Krasucki [19] in the 1950s and 1960s involved electrohydrostatic analyses on droplet deformation. It was assumed that the fluids are perfectly dielectric and mainly accounted for the electric forces normal to the droplet interface. They found that the droplet always deforms into a prolate shape. Taylor [20] and Ajayi [21] proposed the leaky dielectric model, which could account for the electric stresses tangential to the interface and predicted the deformation of a droplet into an oblate shape, as observed in the experiments of Allen and Mason [22]. Tsukada *et al.* [23] and Feng and Scott [24] used a finite element method to study the droplet derformation under

*gtm@iitg.ernet.in

the influence of a uniform electric field using a leaky dielectric model. To study the interaction between a pair of droplets placed in a uniform electric field Baygents *et al.* [25] developed a boundary integral method and applied their formulation to both dielectric and leaky dielectric models. Berry *et al.* [26] simulated conducting drops in a nonconducting medium. Lac and Homsy [27] used a boundary integral method to study the deformation and breakup of a droplet in a uniform electric field and obtained a phase diagram showing the variation of droplet shapes under the influence of different electrical properties. Fernandez and Trygvasson [28] incorporated finite-volume and front-tracking methods to study the behavior of an emulsion of leaky dielectric droplets in an electric field generated by parallel plate electrodes. Fernandez [29,30] did a similar study to investigate the response of an emulsion of a leaky dielectric droplet in a shear flow by employing the same formulation. Hua *et al.* [31] also utilized a front-tracking and finite-volume method to solve the full Navier-Stokes equations and studied the motion of a droplet suspended in a viscous medium under the influence of an electric field. In their work, they considered three different electrical models: a leaky dielectric model, perfect dielectric model, and constant charge model. Zhang and Kwok [32] developed a lattice Boltzmann method employing dielectric theory to study the droplet behavior in a uniform electric field. Sato *et al.* [33] experimentally studied the deformation and breakup of silicone droplets in the presence of an electric field. Timung *et al.* [34] reported a noninvasive way to disintegrate a microdroplet into a string of further miniaturized ones under the influence of an external electrohydrodynamic field inside a microchannel.

The numerous studies discussed above constitute considerable progress towards understanding of the effects of an electric field on droplet motion and deformation in tubes and channels. However, in most of the previous studies, the dynamics was investigated by placing the droplet at the center line of the channel or tube. The cross-stream migration phenomenon of droplets at low Reynolds number in channels still seems to be less explored and needs more attention. Earlier work of Nath *et al.* [16] may also be placed in perspective and extended further. The presence of an electric field also has a profound influence on the droplet migration. Therefore, in the present work, we focus on the dynamics of droplet migration and deformation starting from an initial of-center position and investigate the effect of an electric field on the cross-stream migration phenomenon.

The remainder of the paper is organized as follows: In Sec. II the formulation of the problem is discussed. The details of the computational domain, the pertaining governing equations and the numerical method adopted are mentioned. The qualitative and quantitative validations are conducted to check the accuracy of the mathematical model. This leads to Sec. III, where the results of our computations for a wide range of parameters are discussed. The results include the study of droplet migration in both the absence and presence of an electric field. Finally, concluding remarks are given in Sec. IV.

II. FORMULATION

In this section, we introduce the mathematical model that is employed to study the droplet migration in a 2D channel with and without the influence of an electric field and we examine its accuracy in capturing the flow physics. Figure 1 shows a schematic illustration of the computational domain considered in the present study. The motion of an initially spherical droplet of radius R_0 is placed at a position (x_0, y_0). The hydrodynamics are governed by the incompressible Navier-Stokes and continuity equations, along with an electrohydrodynamic model to describe the electric field effects. The electromechanical coupling occurs at the interface that separates the droplet phase and the suspending fluid, since material and electrical properties are taken to be constant in each phase.

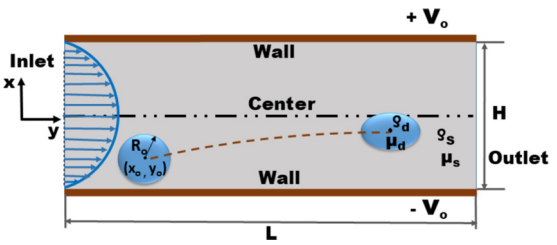

FIG. 1. The schematic representation (not to scale) of the lateral migration of a droplet inside a channel under the influence of external Poiseuille flow and uniform electric field.

A. Governing equations

In the present work, a Newtonian droplet is suspended in another Newtonian medium inside a channel. Both the fluids are considered to be immiscible and incompressible, and the walls of the channel act as electrodes to provide an external DC electrostatic field. A volume-of-fluid approach in the GERRIS framework (see description below) is used. For this problem the governing equations are

$$\nabla \cdot \mathbf{V} = 0, \tag{1}$$

$$\rho[\partial \mathbf{V}/\partial t + (\mathbf{V}\cdot\nabla)\mathbf{V}] = -\nabla P + \nabla\cdot[\mu(\nabla\mathbf{V} + \nabla\mathbf{V}^{\mathbf{T}})] + \gamma\kappa\mathbf{n}\delta + \nabla\cdot\mathbf{M}, \tag{2}$$

$$\partial\alpha/\partial t + \nabla\cdot(\mathbf{V}\alpha) = 0, \tag{3}$$

where $\mathbf{V}(u,v)$ represents the velocity field such that components u, v are along the x and y axis, respectively. The pressure field is denoted by p. The Maxwell's stress tensor for the electric field $\mathbf{M}$ is defined as $\mathbf{M} = \epsilon_o\epsilon_r[\mathbf{E}\otimes\mathbf{E} - \frac{1}{2}(\mathbf{E}\cdot\mathbf{E})I]$. The volume fraction (represented by α) has a value of 1 inside the drop and 0 in the suspending fluid. The surface tension γ effect is considered by incorporating the continuum surface force model of Brackbill *et al.* [35] into the momentum equations. In Eq. (2), κ $(\equiv \nabla\cdot n)$ is the curvature of the interface, wherein $n(\equiv \nabla\alpha/|\nabla\alpha|)$ is the outward pointing unit normal to the interface.

The Gauss law for a perfectly dielectric medium can be written in terms of the electric displacement $(\mathbf{D} = \epsilon\mathbf{E})$ as $\nabla\cdot\mathbf{D} = \nabla\cdot(\epsilon\mathbf{E}) = q_v$. Here ϵ and q_v represent the absolute permittivity of the fluid and the volume density of free charges inside the domain, respectively. For perfect dielectric fluids, no free charge carriers exist $(q_v = 0)$, and hence, the electric

field becomes

$$\nabla \cdot (\epsilon \mathbf{E}) = 0. \tag{4}$$

In the absence of a magnetic field, the irrotational ($\nabla \times \mathbf{E} = 0$) electric field $\mathbf{E}$ employed across the channel can be expressed in terms of the electric potential (V) as $\mathbf{E} = -\nabla V$. Hence, Eq. (4) can be rewritten in terms of electric potential as

$$\nabla \cdot (\epsilon \nabla V) = 0. \tag{5}$$

The electrostatic force acting on the dielectric fluids ($\mathbf{f_e}$) can be represented as

$$\mathbf{f_e} = \nabla \cdot \mathbf{M} = -\tfrac{1}{2}\epsilon_o \mathbf{E} \cdot \mathbf{E} \nabla \epsilon_r, \tag{6}$$

where ϵ_o denotes the permittivity of free space and $\nabla\epsilon$ is the gradient of relative permittivity acting along the interface.

The present study also includes leaky dielectric fluids. The charge conservation equation for such fluids can be expressed as

$$\partial q_v/\partial t + \nabla \cdot (q_v \mathbf{V}) = -\nabla \cdot (\sigma \mathbf{E}). \tag{7}$$

Here σ represents the electrical conductivity of the fluids. The electric relaxation time is given by $t_e = \epsilon/\sigma$, whereas the viscous timescale can be expressed as $t_v = \rho H^2/\mu$. For leaky dielectric fluids, $t_e \ll t_v$ and the charge may accumulate at the interface almost instantaneously as compared to the timescale of fluid motion. Hence, Eq. (7) can be simplified with a quasistatic assumption and expressed as $\nabla \cdot (\sigma \mathbf{E}) = 0$ which can be further converted in terms of electric potential as

$$\nabla \cdot (\sigma \nabla V) = 0. \tag{8}$$

The distribution of volume charge density can be obtained from the Gauss law as $q_v = \nabla \cdot (\epsilon \mathbf{E})$. With the calculated distributions of electric charge density and electric field strength, the electrostatic force ($\mathbf{f_e}$) acting on the leaky dielectric fluids can be written as

$$\mathbf{f_e} = \nabla \cdot \mathbf{M} = -\tfrac{1}{2}\epsilon_o \mathbf{E} \cdot \mathbf{E} \nabla \epsilon_r + q_v \mathbf{E}. \tag{9}$$

The volumed averaged fluid properties are given by

$$\mu = \mu_s \alpha + \mu_d (1 - \alpha), \tag{10}$$

$$\epsilon = \epsilon_s \alpha + \epsilon_d (1 - \alpha), \tag{11}$$

$$\sigma = \sigma_s \alpha + \sigma_d (1 - \alpha). \tag{12}$$

B. Initial and boundary conditions

The following initial and boundary conditions are implemented to solve the governing equations. Initially (at $t = 0$), both the fluids are considered to be at rest [36]. A fully developed velocity profile is imposed at the inlet of the channel ($x = 0$), which is given by

$$u(x) = 1.5 V_{\text{avg}} \left[1 - \frac{y^2}{(H/2)^2}\right] \quad \text{and} \quad v(x) = 0, \tag{13}$$

where V_{avg} is the average velocity of the imposed flow. The no-slip and no-penetration conditions ($u = v = 0$) are imposed at the channel walls, i.e., $y = \pm H/2$. At the outlet of the channel ($x = L$), the Neumann boundary conditions for the velocity components and fixed pressure condition are applied and given by

$$\frac{\partial u}{\partial x} = \frac{\partial v}{\partial x} = 0 \quad \text{and} \quad p = p_0. \tag{14}$$

The external electric field is applied by imposing constant voltage boundary conditions $V = +V_o$ and $V = -V_o$ at the upper and lower walls of the channel, respectively.

C. Numerical method

A finite volume open source computer code, GERRIS [37], is used for studying the dynamics of drop motion and deformation inside a microchannel. A volume-of-fluid method with added capabilities of reduction in spurious currents at the interface makes it suitable and appropriate for simulating fluid flows with interface and has been used by many researchers successfully in solving complex fluid flow problems [38–41]. Additionally, for the two-phase electrohydrodynamic simulations, GERRIS was chosen because the electrohydromodule [42] of GERRIS is capable of solving the incompressible Navier-Stokes equations coupled with an electric potential and electric charge density accurately [43,44]. Moreover, GERRIS is equipped with dynamic adaptive mesh refinement ability that allows more computational cells to be used near the desired regions dynamically [37]. All the features discussed above are advantageous for the present simulations.

D. Nondimensionalization

The results obtained from the numerical simulations are presented in terms of dimensionless parameters. The height of the channel, H, and average imposed velocity, V_{avg}, are used as the length and velocity scales, while μ_s is used as the viscosity scale. The aspect ratio, a^*, defined as the ratio of the initial droplet diameter to the height of the channel, is given by $2R_0/H$. The chosen reference quantities give rise to the following set of dimensionless parameters:

$$\text{Ca} \equiv \frac{\mu_s V_{\text{avg}}}{\gamma}, \quad \text{Re} \equiv \frac{\rho_s V_{\text{avg}} H}{\mu_s}, \quad \lambda = \frac{\mu_d}{\mu_s},$$
$$S = \frac{\epsilon_d}{\epsilon_s}, \quad R = \frac{\sigma_d}{\sigma_s}, \quad E^* = \frac{E}{V_{\text{avg}}}\sqrt{\frac{\epsilon_s}{\rho_s}}. \tag{15}$$

The parameters in Eq. (15) correspond to the capillary number, Reynolds number, viscosity, permittivity, and conductivity ratios, and a dimensionless electric field, respectively. Here E_c is the characteristic scale for electric field strength given as $E_c = V_{\text{avg}}\sqrt{\rho_s/\epsilon_s}$. The seemingly uncommon scaling for electric field is stimulated by the numerical work and is adopted so that the dimensionless parameter associated with the Maxwell stresses in Eq. (2) is unity. For the sake of convenience, E^* is represented as E for the rest of the paper and denotes the dimensionless electric field strength. In the present study, the Reynolds number is assumed to be small (Re $= 1$), i.e., the influence of inertia force can be assumed to be negligible compared to the viscous force. Furthermore, we study the migration of a neutrally buoyant droplet in the simulations, and the results are presented in terms of dimensionless time, $t^* \equiv t V_{\text{avg}}/H$. We also introduce a dimensionless term y_c, which represents the lateral position

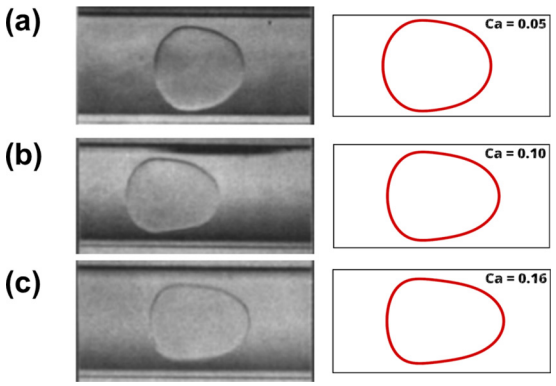

FIG. 2. Comparison of drop shape for three different Ca: 0.05, 0.10, and 0.16. The other parameters are $a^* = 0.95$ and $\lambda = 0.99$. Left panel: Experimental results [4]; right panel: present simulations.

(area-averaged center) of the droplet in the channel. The value of the y_c ranges between -0.5 and $+0.5$. The length of the channel is considered to be $L = 40H$.

E. Validation

1. Qualitative comparisons

For the purpose of validation, we compare our simulation results with the experimental results of Olbricht and Kung [4] for a drop of size $a^* = 0.95$ suspended in a system with $\lambda = 0.99$. Note that those authors investigated the dynamics of droplet migration in a capillary tube, unlike in a 2D channel as considered in the present study. Three different Ca are considered: 0.05,0.10, and 0.16. Figure 2 depicts that the present computational results possess a good qualitative match with their experimental counterpart.

2. Quantitative comparisons

To examine the accuracy of the present numerical solver for electrohydrodynamic simulations, the deformation of a spherical drop suspended in a stationary fluid is examined. The deformation is characterized by the Taylor's deformation parameter $D = \frac{L-B}{L+B}$, where L and B are the end-to-end length of the droplet measured along the x and y directions, respectively. A positive D represents the deformation along the field direction (prolate shape), whereas a negative D represents the deformation perpendicular to the field direction (oblate shape); $D = 0$ represents a spherical droplet. The analytical solution for the drop deformation under electric field provided by Taylor [20] is given by

$$D = \frac{9\mathrm{Ca}_E}{8(2+R)^2}\left[R^2 + 1 - 2S + \frac{3}{5}(R-S)\frac{2+3\lambda}{1+\lambda}\right], \quad (16)$$

where $\mathrm{Ca}_E = \frac{E^2\epsilon_o R_o}{\gamma}$ is defined as the electrical capillary number, which signifies the relative strength of the external electric field over capillary force.

Figure 3 presents a quantitative comparison between the theoretical prediction of Eq. (16) and the results obtained from our current simulations. A good agreement can be observed for the deformation parameter D under varying conditions of Ca_E and R from Figs. 3(a) and 3(b), respectively.

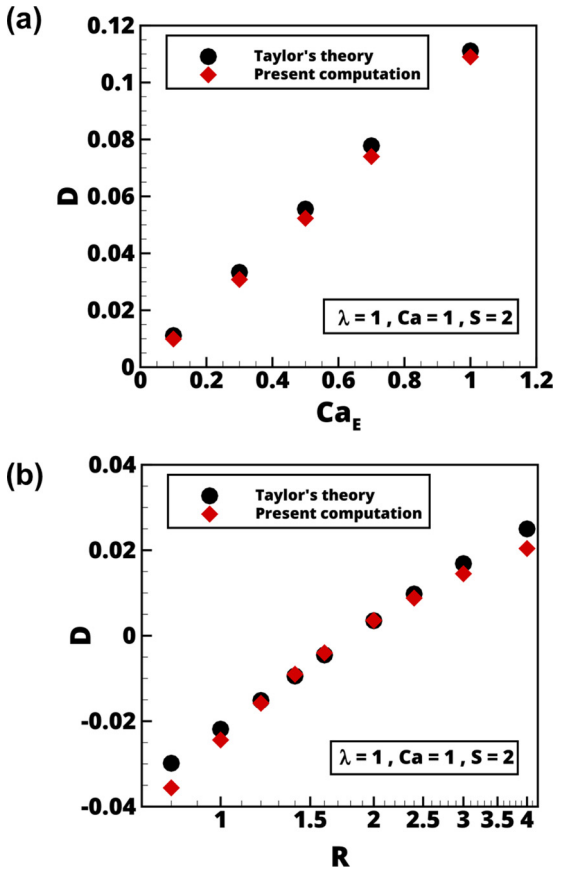

FIG. 3. Comparison of drop deformation computed from the present simulations with Taylor's theory [Eq. (16)] for varying Ca_E and R, respectively.

3. Grid independence test

The grid convergence test is conducted by simulating the migration of a droplet in a channel with aspect ratio $a^* = 0.6$. The rest of the dimensionless parameters are $\mathrm{Ca} = 0.7$ and $\lambda = 1.0$. The adaptive mesh refinement feature of GERRIS is employed to increase the grid density near the interfacial region while maintaining a relatively coarser mesh elsewhere. The refinement is done based on the gradient of volume fraction. Figure 4(a) presents snapshots of different levels of refinement deployed for the grid convergence test. The smallest (dimensionless) cell sizes are 0.031, 0.016, 0.008, and 0.004 corresponding to grid levels 5, 6, 7, and 8.

The temporal variations of the drop y_c for different grid refinement levels are presented in Fig. 4(b). It is observed that the drop y_c measured at $t^* = 15$ differs by ∼50% between levels 5 and 6 and by ∼11% between levels 6 and 7, whereas the difference between levels 7 and 8 is less than ∼3%. In view of this, and optimizing the computational time and cost without compromising the accuracy of the results, grids with refinement level 7 are used to generate the rest of the results presented in this study.

F. Fluid properties

The drops can be considered to be composed of silicon oil and the suspending medium comprising castor oil. Different

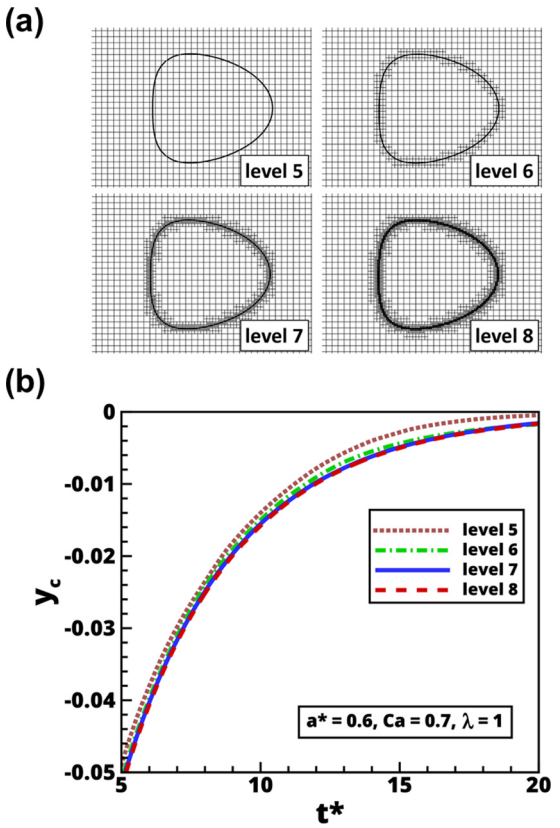

FIG. 4. Grid convergence test. (a) Snapshots of adaptive mesh generation using different levels of refinement. The refinement level of 7 is selected for the present study. (b) Comparison of y_c for different levels of grid refinement. The different parameters considered are $a^* = 0.6$, Ca $= 0.7$, and $\lambda = 1.0$.

grades of silicon oil help us to get different viscosity ratios required for the parametric studies [45]. For perfect dielectric fluids, s silicon oil droplet in a medium of castor oil or vice versa can be considered depending on the permittivity ratio. For leaky dielectric fluids, two system of fluids are considered. System *A* represents a drop whose permittivity is lower but conductivity is higher than that of the suspending medium. System *B* represents a drop whose permittivity is higher but conductivity is lower than that of the suspending medium. Such fluid properties can be obtained by considering a silicone oil drop in castor oil medium for system *A* and a castor oil drop in a silicone oil medium for system *B* [46]. The conductivity of silicone oils can be increased using doping in order to obtain a large range of conductivity ratio, *R* [46].

III. RESULTS AND DISCUSSION

The lateral migration phenomenon of a drop inside a microchannel is studied in both the absence and presence of an electric field and are discussed in Secs. III A and III B, respectively. The cross-stream locomotion of a drop placed off-center inside a channel for low Reynolds number flows can be attributed to the shape deformation of the drop under the influence of the incident flow and the variation of shear stress acting across the drop. The shape deformation leads to an aerodynamically favorable shape for the drop to move towards the center line. The deformation is more prominent for larger drops which undergo larger shape deformation. A similar mechanism was thoroughly discussed in Karimi *et al.* [47] in the context of cell migration in microfluidics. Owing to the proximity of an off-center drop to the channel wall, the influence of shear force is significant, and the variation of shear stress across the drop leads to the migration of the drop from the initially released position to an equilibrium position. Additionally, the rotation of the drop can result in the generation of Magnus lift force and the strength of this force is dependent on the angular velocity of the spinning droplet. The rotational effect has been found to be negligible for a significant portion of this study. However, the application of an external electric field under certain conditions may result in strong rotation of the drop as it traverses across the channel. The lift force generated by the Magnus effect assumes significance in such flow conditions.

A. Drop dynamics under the influence of Poiseuille flow without electric field

The dynamics of drop deformation and lateral migration in the Poiseuille flow in a microchannel (in the absence of electric field) are dictated by the relevant nondimensional parameters: drop size (a^*), capillary number (Ca), and viscosity ratio (λ). Therefore, the effect of each one of these parameters for a drop placed at an off-center position is discussed in this subsection.

1. Effect of drop position

To understand the effect of the initial position of the drop on its migration phenomenon, a drop of moderate size ($a^* = 0.6$) was placed at different off-center positions along the y axis. The capillary number and viscosity ratio were considered to be 0.7 and 1, respectively. Over a wide range of initial positions of the drop, it is observed that the drop moves away from the channel walls and drifts towards the center line and attains a steady bullet shape with the drop center lying in the channel center line. For the set of parameters, this phenomenon is observed to be consistent regardless of the initial off-center placement of the drop. Figure 5(a) shows the migration of the drop towards the channel center from different off-center positions. Mortazavi and Tryggvason [13] showed that the migration of a small drop towards or away from the wall depends on the viscosity ratio between the drop and medium, but for the moderate size drops suspended in systems with matching viscosities, the drops always tend to migrate towards the channel center. A similar dynamics was also observed by Griggs *et al.* [11] and Coulliette and Pozrikidis [10]. During its movement to the channel center, the drop undergoes shape deformations and finally attains a steady bulletlike shape.

The streamlines in and around the drop placed at $y_c = 0$, -0.1, and -0.15 are shown in Fig. 5(b). The images are taken at $t^* = 5$. At this particular time instant, the drop placed initially at the center line ($y_c = 0$) has already reached a steady bulletlike shape and moves with a steady velocity. However, the drops placed at off-center positions have not attained a steady bullet shape; rather, they are observed to be laterally migrating towards the channel center line while traversing in the axial direction. It is clearly evident from Fig. 5(a) for the drop placed initially at $y_c = -0.15$ that the prominent vortices

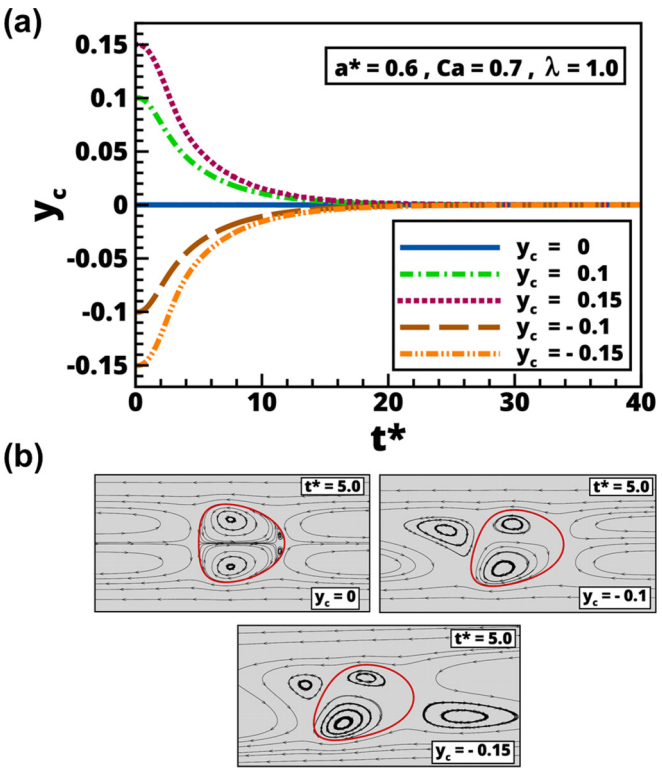

FIG. 5. A drop ($a^* = 0.6$) initially placed at different off-center positions gradually migrates towards the center line of the channel. The other parameters are Ca = 0.7 and $\lambda = 1$. (a) The lateral position of the drop versus time. (b) The streamlines around the drop placed at $y_c = 0$, -0.1, and -0.15, respectively. The flow field is presented in the frame of reference of the drop.

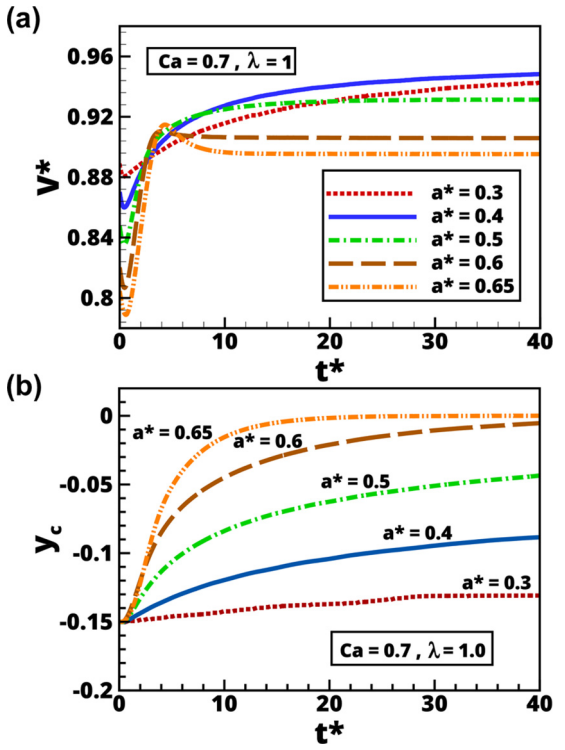

FIG. 6. Migration of different sized droplets starting from an initial off-center position ($y_c = -0.15$) towards the channel center line. (a) Drop velocity versus time. (b) Lateral position versus time. The other parameters are Ca = 0.7 and $\lambda = 1$.

formed around the drop promote the lateral deformation and push the drops to drift towards the channel center line. Though a little less pronounced, this phenomenon is also seen to be exhibited well by the drop placed initially at $y_c = -0.1$.

The confined flow inside a microchannel results in a sharp gradient of velocity across the channel cross section, and the shear force is stronger close to the walls. The initial migration rate [slope of y_c versus t^* in Fig. 5(a)] of a drop for initial $y_c = \pm 0.15$ is higher than that observed for initial $y_c = \pm 0.1$. This can be attributed to the larger shear variation experienced by such drops. As the drop approaches the center line, the shear force acting on the drops decreases and the migration rate attains a smaller value for both values of y_c considered. Furthermore, the shear force on the drop can also be tuned by manipulating the drop size and the capillary number as well as the viscosity ratio, which can result in significant modification of the shape deformation as well as the shear force, thereby affecting the dynamics of the migration process. The influence of drop size, capillary number, and viscosity ratio is discussed in the following sections.

2. *Effect of drop size*

The size of the drop plays a vital role in its migration phenomenon. To understand the effect of drop size, simulations are performed for drops of varying sizes in the range $a^* = 0.3$ to 0.65. All the drops are released from an initial position that is below the center line ($y^* = -0.15$) of the channel. The other parameters considered are Ca = 0.7 and $\lambda = 1$. The effect of size on the drop migration is shown in Fig. 6. For the range of drop sizes considered, and under the given set of conditions, it is observed that all the drops move away from the wall. The temporal variations of drop velocity are plotted in Fig. 6(a) for five different drop sizes ranging from $a^* = 0.3$ to 0.65. Figure 6(b) shows the variations of the corresponding lateral position of the drop with time. It is seen that the large drops have a higher tendency to migrate towards the channel center line. For $a^* = 0.65$, the drop reaches the channel center line and attains a steady shape and velocity. However, smaller drops do not seem to attain a steady lateral position within the length of the channel under consideration. A possible explanation of this is as follows: big drops are associated with enhanced shape deformation, which makes the drops aerodynamically favorable to move towards the center line of the channel. In contrast, this aerodynamic deformation is absent in the case of small drops as they remain spherical due to the effect of larger surface tension force as compared to bigger drops.

The smallest drop $a^* = 0.3$ exhibits very less lateral migration and seems to settle down at a lateral position very close to the initial off-center position. The intermediate drops $a^* = 0.4$ and 0.5 settle at a lateral position that is somewhere between the channel center line and the initial off-center position. The varied dynamics exhibited by different sized drops can be explained as follows. As the droplet size increases, the equilibrium position of the drop moves closer to the center line of the channel. The variation of shear stress acting across

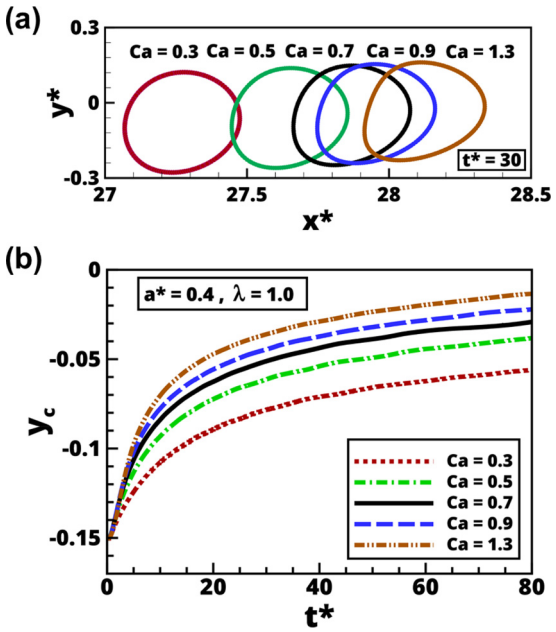

FIG. 7. The effect of varying Ca (Ca = 0.3 to 1.3) on the migration of a drop initially placed at $y_c = -0.15$. (a) Drop velocity versus time. (b) Lateral position of the drop versus time. The other parameters are $a^* = 0.4$ and $\lambda = 1$.

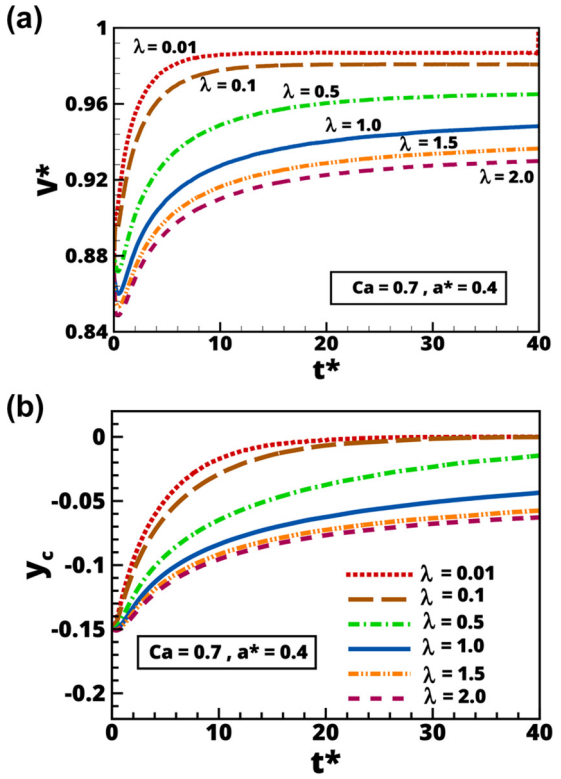

FIG. 8. The effect of varying viscosity ratio ($\lambda = 0.01$ to 2.0) on the migration of a drop initially placed at $y_c = -0.15$. (a) Drop velocity versus time. (b) Lateral position of the drop versus time. The other parameters are $a^* = 0.4$ and Ca = 0.7.

the drop increases with increasing size of the drop, which leads to faster migration of a large drop towards the center line in comparison to a smaller drop as depicted by Fig. 6. Thus, large drops deform more and advect away from the wall at a faster rate than smaller drops for a given pressure drop. It is also observed in Fig. 6(a) that the smaller drops move with a higher velocity in the channel as compared to the larger drops. For the length of the channel under consideration, drops with $a^* = 0.5, 0.6$, and 0.65 reach a steady velocity, but the smaller drops of sizes $a^* = 0.3$ and 0.4 do not attain a steady velocity. Figure 6(b) reveals that for the given length of the channel ($L^* = 40$) the smaller drops ($a^* = 0.3, 0.4$) do not reach the center line of the channel, while the larger drops reach the channel center line quite early.

3. *Effect of capillary number*

The drop migration is influenced immensely by the capillary number. A higher value of capillary number is led by a lower surface tension force and dominating viscous force. Thus, with the increase in the capillary number, the ability of the drop to deform increases, which in turn leads to an enhanced rate of cross-stream migration of the drop.

This phenomenon is evident in Fig. 7, where the effect of Ca on drop migration is investigated for a drop of size $a^* = 0.4$. Ca is varied from 0.3 to 1.3 and the viscosity ratio is taken as 1. Figure 7(a) shows the drop shape and position at $t^* = 30$ for different values of Ca. It is seen that at the same time instant ($t^* = 30$) the drop occupies different positions and assumes different shape under the influence of varied Ca. It is evident from Fig. 7(a) that with the increase in Ca, the drop evolves from a nearly spherical shape to a more deformed shape with a lift in their lateral position. Even though we have used a channel length of $40H$ in all the investigations, Fig. 7 was especially investigated for a channel length of $80H$ over a longer duration ($t^* = 80$). Longer time simulations depict that the drops do not reach the center line.

4. *Effect of viscosity ratio*

The viscosity ratio of the drop fluid to the suspending fluid also plays a vital role in drop migration. In this section, we examine the effect of viscosity ratio on the lateral migration of a drop of size $a^* = 0.4$. The value of Ca is taken as 0.7, and λ is varied from 0.01 to 2.0. Figure 8(a) depicts the influence of viscosity ratio on the velocity of the drop while traversing in the channel. It is observed that when Ca is fixed, with the increase in viscosity ratio, the velocity of the drop decreases owing to the increased hydrodynamic resistance. In Fig. 8(b), the temporal variations of the center position of the drop is plotted. It is observed that all the drops tend to migrate towards the channel center line. Once a drop reaches the channel center line, it moves with a steady velocity maintaining a bulletlike shape. The deformation of the drop is dictated by the capillary number as well as the viscosity ratio, and their dominance over each other decides the rate at which the drops migrate towards the channel center line. As the viscosity ratio is increased, the lubricating effects between the wall and the drop are reduced. The drop fails to drift towards the channel center line easily and tends to settle down in a lateral position that lies somewhere between the channel center line and the initial off-center position of the drop.

As shown in Fig. 5(b), it is also clear that the migration towards the center line from different off-center positions are associated with asymmetrical shape deformation of the droplet. For very low values of Ca, the drop does not deform much (tends to retain its spherical shape) due to the effect of high surface tension (Fig. 7). Thus the lateral migration of the droplet can be suppressed for small values of Ca (in the surface tension-dominated regime). It is also observed that the drops of small size undergo less deformation (Fig. 6). For fixed values of other parameters, increasing the viscosity ratio, λ, would again have a similar effect as that of increasing surface tension (Fig. 8). Therefore, intuitively we can conclude that the lateral migration of a moderate-sized droplet decreases with decreasing Ca and increasing λ.

B. Drop dynamics under the influence of Poiseuille flow with an electric field

As mentioned in Sec. II, the presence of an electric field introduces an additional stress at the interface, termed the Maxwell stress. The interfacial force may aid or oppose the surface tension force depending upon the sign of radius of curvature of the interface. The shape of the drop is influenced by the resultant effect of surface tension, Maxwell stress, and viscous stresses. In this subsection, we consider perfect dielectrics, where free charge carriers do not exist and electric stresses act normal to the interface. Also, we consider leaky dielectrics (poor conductors) that support accumulation of interfacial charges implying the presence of tangential stresses. The deformation and migration of the droplet in the presence of an electric field are significantly affected by the electric properties of the fluid, namely, permittivity, resistivity, and conductivity.

1. *Dielectric fluids: Effect of permittivity ratio*

The effect of the permittivity ratio on the lateral migration of a drop ($a^* = 0.4$) is studied by varying the permittivity ratio (S) of the dispersed fluid to continuous fluid between 0.2 and 5.0. The other parameters are fixed at Ca $= 0.7$, $\lambda = 1$, and the electric field strength, $E = 5$. Figure 9(a) shows the shapes attained by the drop for different permittivity ratio at $t^* = 30$. It is clearly seen that as the permittivity ratio increases, the shape of the drop changes significantly. At high permittivity ratio, the drop takes a convex shape at the front and a concave shape at the back. This is because the higher dielectric permittivity of the drop fluid as compared to the suspending medium leads to the accumulation of a large number of induced bound charges across the interface, which generates the electrohydrodynamic stress to elongate the droplet towards the electrodes and form the plug inside the channel. Figure 9(b) shows that with the increase in permittivity ratio the lateral migration of the drop increases quite monotonically. However, it is also observed that as the permittivity ratio is increased, beyond $S = 3$, the drop overshoots the equilibrium position and oscillates several times around the mean position. These oscillations are more pronounced for $S = 5$ where the oscillations gradually dampen. However, the oscillations do not die down completely within the channel length of interest. In Fig. 9(a) it can be seen that highly deformed droplet shapes are formed for $S = 4.0$ and 5.0, and these critical shapes lead to oscillations of the drops around its equilibrium position.

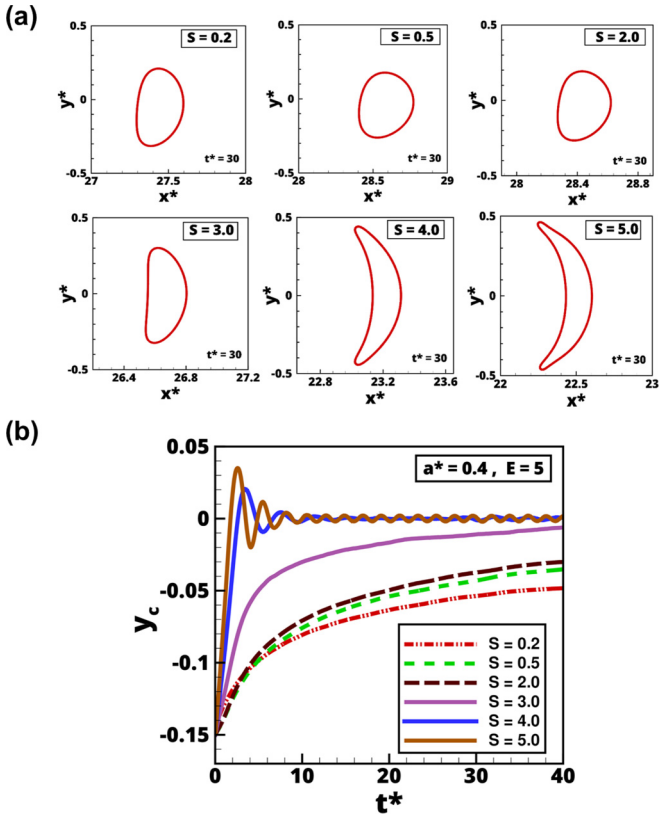

FIG. 9. Effect of varying permittivity ratio ($S = 0.2$ to 5) on the deformation and migration of a drop initially placed at $y_c = -0.15$. (a) The shape of a drop at $t^* = 30$ subjected to different permittivity ratio S. (b) The lateral position of the drop versus time. Other parameters are $a^* = 0.4$, Ca $= 0.7$, $\lambda = 1$, and $E = 5$.

The normalized pressure drop over the channel is shown in Fig. 10(a) for $S = 0.2$ to 5.0 at $t^* = 30$. The dashed line in Fig. 10(a) represents the normalized pressure drop in the

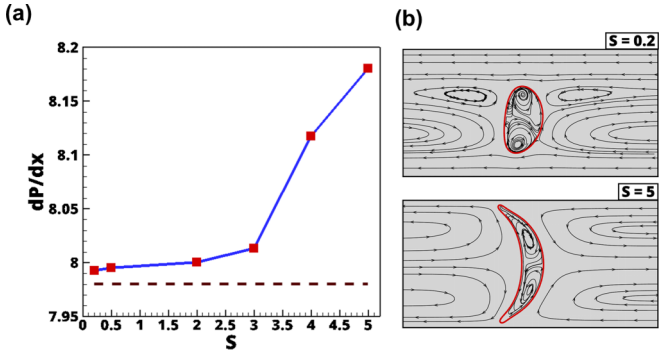

FIG. 10. Effect of elongation of the drop. (a) The normalized pressure drop in the channel for different permittivity ratio compared to the pressure drop in the channel in the absence of any drop (dashed line). (b) The streamlines around a drop subjected to varying permittivity ratio ($S = 0.2$ and 5) at $t^* = 30$. The flow field is presented in the frame of reference of the drop. Other parameters are $a^* = 0.4$, Ca $= 0.7$, $\lambda = 1$, and $E = 5$.

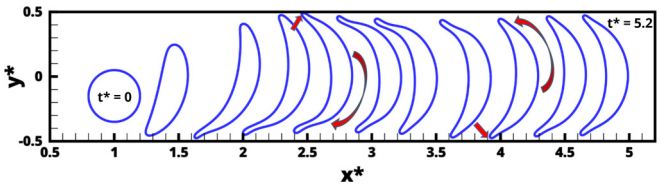

FIG. 11. Variations of shape a drop ($a^* = 0.4$) initially placed at $y_c = -0.15$ inside the channel and subjected to electric field from $t^* = 0$ to 5.2. The other parameters are Ca = 0.7, $\lambda = 1$, $E = 5$, and $S = 5$.

channel in the absence of any drop. It is observed that as the drop undergoes elongation and gradually occupies the entire cross section of the channel, the pressure drop inside the channel increases. The streamlines in and around the drop are plotted for the two extreme cases, for $S = 0.2$ and 5.0, as shown in Fig. 10(b). For higher value of S, the deformation of the drop leads to a lobelike shape yielding a higher blockage ratio. The streamlines described by the channel fluid reveal a typical situation corresponding to flow past a bluff body inside a channel. The near wake region broadens with the increase in blockage ratio.

The reason behind the drop oscillations about the mean position observed in Fig. 9(b) for $S = 4$ and 5 can be better explained by analyzing Fig. 11, which illustrates the evolution of a liquid lobe. In Fig. 11 the motion of a drop of $a^* = 0.4$ is shown for $t^* = 0$ to 5.2 when subjected to $E = 5$ and $S = 5$. It is observed that the drop stretches and takes a bow shape rapidly as it starts moving in the channel. But the drop during its motion inside the channel hits the top and bottom wall surfaces, alternatively (as shown by the red arrow). Thus the phenomenon of oscillations of the drop mean position [as witnessed in Fig. 9(b) for $S = 5$] is exhibited because when the drop hits a wall, an opposite and equal force is exerted by the wall on the drop which makes it move away from that surface laterally while it is still in axial motion. As the drop continues to rebound after hitting the wall, it gradually travels across the channel and hits the opposite wall, and this event continues. The oscillations of drop mean position are higher at the beginning [as observed in Fig. 9(b) for $S = 5$] due to the instability caused by the onset of drop deformation; however, as the drop gradually takes a steady shape, the oscillation is found to be varying about a mean position $y_c = 0$ (center line).

2. *Dielectric fluids: Effect of electric field strength*

To understand the effect of electric field strength E on the migration of a given drop ($a^* = 0.4$), E is varied from 5 to 20. Figure 12(a) depicts the influence of E on the shape of the drop. The images show the deformed shape of the drop at a particular time instant $t^* = 30$. The steady shapes obtained by the drop subjected to different E clearly reveal that with the increase in E, the drops get highly stretched and elongated in the direction of the electric field. Figure 12(b) shows the lateral position of the drop while moving inside the channel subjected to varied E.

It is observed that, for all other parameters remaining fixed, a drop under the influence of a high value of E ($E = 15$ and 20) drifts faster towards the channel center line and

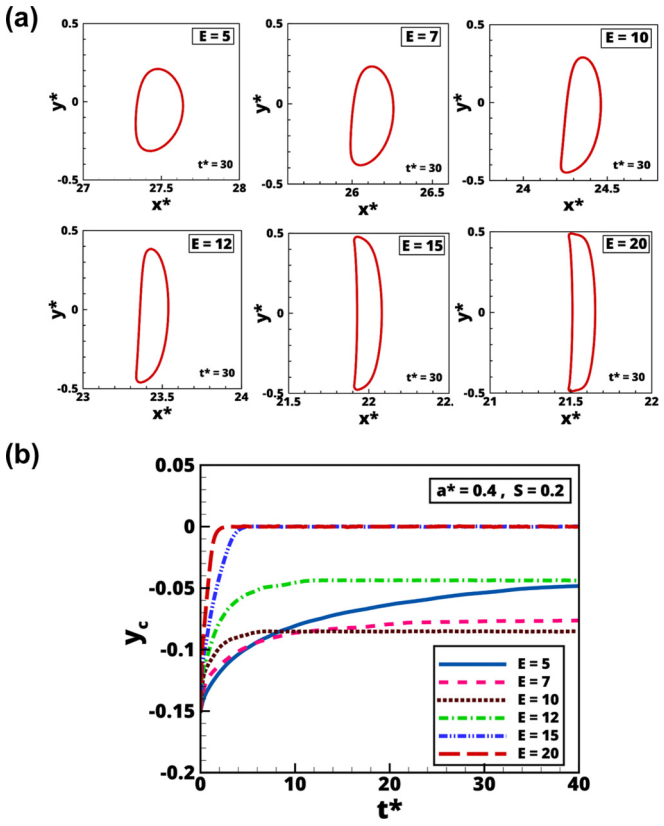

FIG. 12. Effect of varying electric field strength ($E = 5$ to 20) on the deformation and migration of a drop initially placed at $y_c = -0.15$. (a) The shape of a drop at $t^* = 30$ subjected to different E. (b) The lateral position of the drop versus time. Other parameters are $a^* = 0.4$, Ca = 0.7, $\lambda = 1$, and $S = 0.2$.

attains a steady velocity and hence a steady lateral position. Whereas for intermediate values of E ($E = 10$ and 12) the drop attains a steady lateral position somewhere between the initial off-center position and the channel center line. This trend is seemingly followed by the drop subjected to $E = 7$ somewhere downstream. On the other hand, a drop subjected to a lower value of E ($E = 5$) does not reach a steady lateral position for the channel length of interest, and it is evident that it exhibits quite less cross-stream migration. For $E > 10$, due to large elongation in the direction of electric field (the drop tends to completely occupy the channel), the drop becomes symmetrical about the $y^* = 0$ axis. Thus the center of gravity of the drop moves to the center line of the channel. On the other hand, there is a combined influence of asymmetrical shape deformation and the electric field for $E < 10$, which results in an unsteady state till later times and prevents the drop from moving to the center line. For this set of parameters, this transition is occurring for $E = 10$, thereby resulting in a nonmonotonic trend around $E = 10$.

The normalized pressure drop over the channel is shown in Fig. 13(a) for $E = 5$ to 20 at $t^* = 30$. The dashed line in Fig. 13(a) represents the normalized pressure drop in the channel in the absence of any drop. It is seen that as the drop gets more and more stretched in the presence of a high electric field strength, the pressure drop inside the channel increases. The streamlines in and around the drop are plotted

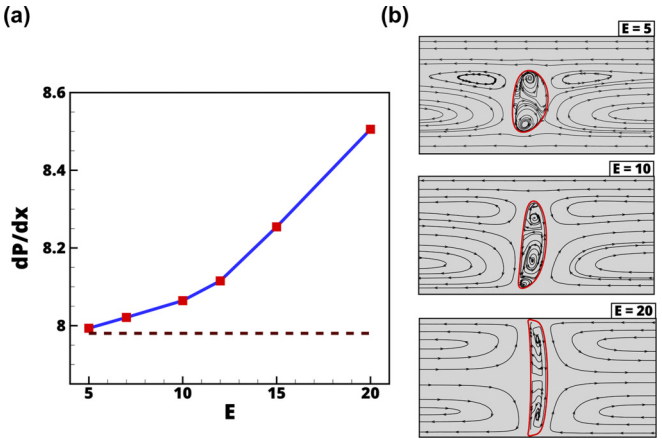

FIG. 13. Effect of elongation of the drop. (a) The normalized pressure drop in the channel for different electric field strength compared to the pressure drop in the channel in the absence of any drop (dashed line). (b) The streamlines around a drop subjected to varying electric field strength ($E = 5$, 10 and 20) at $t^* = 30$. The flow field is presented in the frame of reference of the drop. Other parameters are $a^* = 0.4$, Ca $= 0.7$, $\lambda = 1$, and $S = 0.2$.

for $E = 5$, 10, and 20,as shown in Fig. 13(b). In the case of $E = 20$, the stretched drop assumes almost the shape of a vertical elongated body occupying more than 98% of the flow area. Immediately downstream is fully occupied by the separated symmetrical eddies. The approach flow streamlines resemble the streamlines of stagnation flow.

3. Leaky dielectric fluids

To study the effect of conductivity ratio R together with permittivity ratio S and electric field strength E and to understand the result of their dominance over each other on the droplet migration, we consider the fluids to be leaky dielectric. Two different systems are considered, namely, system A in which the drop fluid is more conducting than medium fluid, while permittivity of the medium fluid is higher than the drop fluid ($S = 0.5$ and $R = 2$), and system B, which has the exactly opposite combination ($S = 2$ and $R = 0.5$). E is varied from 1 to 5. Figures 14(a) and 14(b) show the shapes of the more conducting and less conducting drops, respectively, at $t^* = 30$ for varying E.

In Fig. 15 it is seen that in system A ($S = 0.5$ and $R = 2$), the drop migrates nearly monotonically towards the channel center line (shown by the dotted lines). As E increases from 1 to 5, the drop attains a steady lateral position faster. However, for system B ($S = 2$ and $R = 0.5$), Fig. 15 (solid lines) reveals that the drop does not reach the channel center line but settles at a lateral position close to its initial position. It is also observed in the case of system B that with the increase in E from 1 to 3, the drop moves along a steady y_c. However, with further increase in electric field strength $E = 4$ and 5), it is seen that the lateral position of the drop oscillates around a mean value for some time. These oscillations are depicted because the drop along with translational motion now also exhibits rotational motion. This phenomenon is more pronounced for $E = 5$ as compared to $E = 4$. The oscillations gradually dampens with time, in both cases.

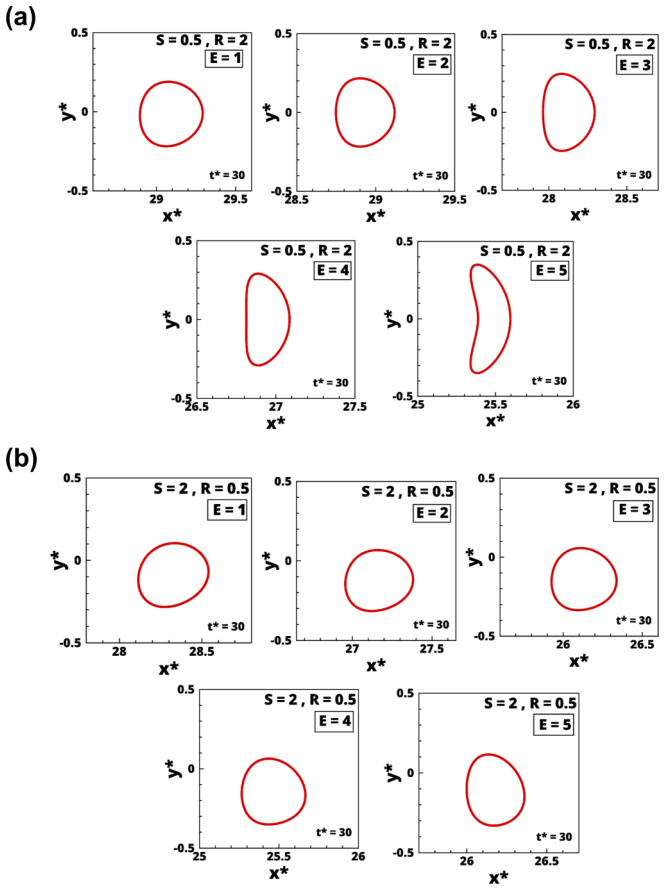

FIG. 14. Shapes of the drop at $t^* = 30$ while migrating from an initial off-center position of $y_c = -0.15$ and subjected to different permittivity ratio S, conductivity ratio R, and electric field strength E. (a) Drops suspended in a system of $S = 0.5$ and $R = 2$ and subjected to varying E. (b) Drops suspended in a system of $S = 2$ and $R = 0.5$ and subjected to varying E. E is varied in the range of 1 to 5. Other parameters are $a^* = 0.4$, Ca $= 0.7$, and $\lambda = 1$.

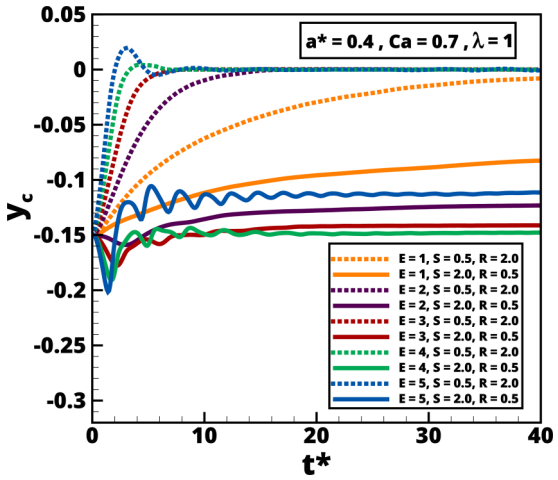

FIG. 15. The migration of a drop initially placed at $y_c = -0.15$ towards the center line of the channel influenced by different electric field strength E, permittivity ratio S, and conductivity ratio R. Dotted and solid lines represent the position of the drop suspended in systems A and B, respectively. Other parameters are $a^* = 0.4$, Ca $= 0.7$, and $\lambda = 1$.

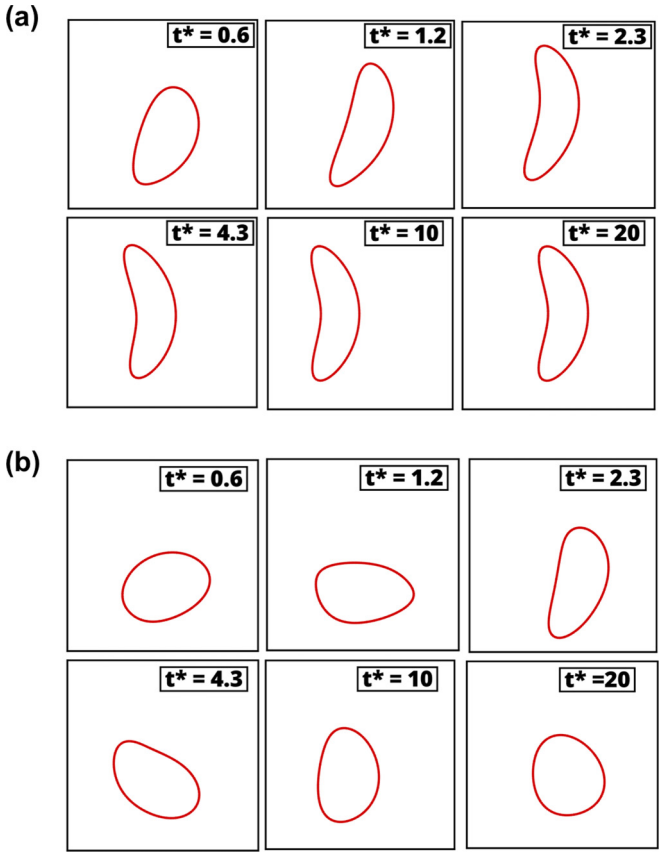

FIG. 16. The transient evolution of a drop ($a^* = 0.4$) initially placed at $y_c = -0.15$ inside the channel. For system A (a) and B (b). The other parameters are Ca = 0.7, $\lambda = 1$, and $E = 5$.

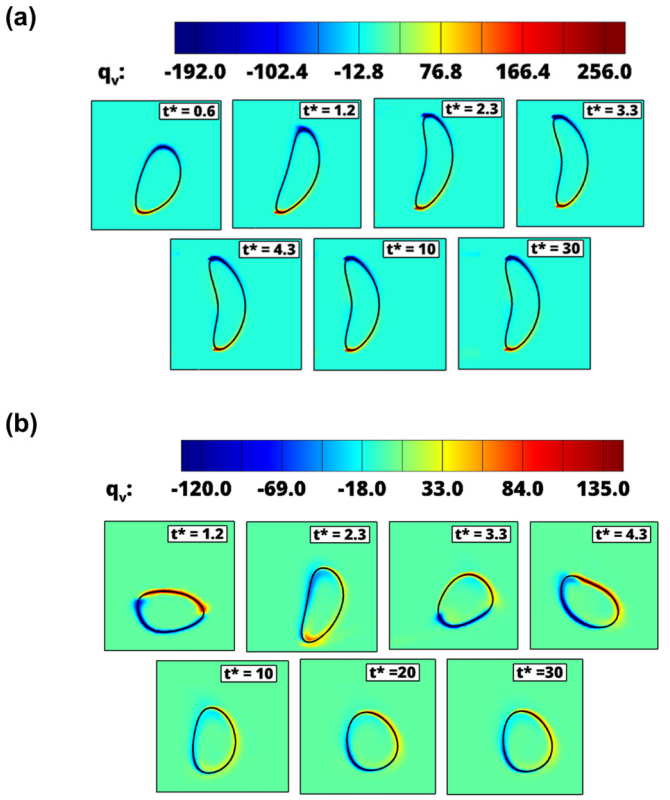

FIG. 17. The charge density at the interface of a drop ($a^* = 0.4$) initially placed at $y_c = -0.15$ inside the channel subjected to electric field. (a) Charge distribution at the interface of a nonrotating drop suspended in system A. (b) Charge distribution at the interface of a rotating drop suspended in system B. The other parameters are Ca = 0.7, $\lambda = 1$, and $E = 5$.

Taylor provided the analytical solution for drop deformation under an electric field as given in Eq. (16), and it is observed that for $R < S$, the deformation is negative, i.e., the drop attains an oblate shape. However, for $R > S$, $D > 0$ and the drop becomes prolate. Thus, the relative magnitudes of R and S play the dominant role in deciding the drop deformation, behavior, and subsequently the migration dynamics.

The influence of R and S on the migration characteristic of the drop is amply demonstrated in Figs. 16(a) and 16(b) for a drop ($a^* = 4$) migrating under the influence of $E = 5$ suspended in systems A and B, respectively. The transient evolution of the drop suspended in both systems is shown from $t^* = 0.6$ to 20. A snapshot at $t^* = 0.6$ for system A ($R > S$) as shown in Fig. 16(a) clearly depicts the prolate deformation, whereas for the same time instant the deformation is oblate for system B ($R < S$) as observed in Fig. 16(b). The electric force acting on the two sides of the drop is different in case of a nonrotating and a rotating droplet. Figure 17 shows the charge density at the interface of a migrating drop suspended in systems A and B, respectively, at different time instants under the influence of $E = 5$. The upper electrode of the channel is at a positive potential of +V, whereas the lower electrode is at a negative potential of V. The plots in Fig. 17(a) demonstrate that the charge accumulation in system A is opposite to the direction of the applied electric field. The charge accumulated at the top of the drop for system A is negative, whereas at the lower portion of the drop, positive charge accumulates. The opposite nature of charge between the electrodes and the drop interface results in a pulling force on the drop which leads to an equilibrium position at the center line. However, the charge accumulation for system B, shown in Fig. 17(b), is different from system A with positive charge at the top and negative charge at the bottom of the drop interface (as can be seen for $t* = 1.2$). This results in a compressive force on the drop and leads to an off-center equilibrium position. It is to be noted that the drop placed off-center migrates towards an equilibrium position as discussed in Sec. III A, and the prolate deformation (system A) assists the migration of the drop towards the center of the channel. The deformation is further enhanced at higher field strength thereby further accelerating the migration rate as is clearly evident in Fig. 15 for the dotted lines. In contrast, for system B, the drop deforms in the oblate direction, and the oblate shape being hydrodynamically unfavorable undergoes a series of rotations to attain a favorable shape at steady state. As observed from the solid lines in Fig. 15, this phenomenon of rotation is more pronounced under the influence of high E.

Another reason for the rotational motion is that the drops having higher permittivity ratio and lower conductivity ratio (system B) when subjected to a high electric field ($E = 4$ or 5) deform initially in the direction of the field. This results in a slight decrease in the magnitude of y_c during the early stages of migration as can be seen for $t^* \leqslant 3$ in Fig. 15. However,

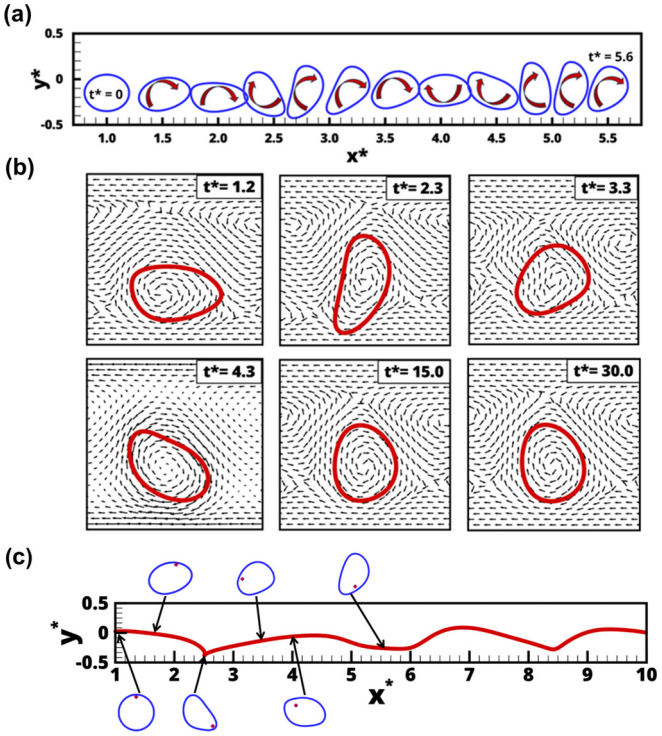

FIG. 18. The rotation of a drop ($a^* = 0.4$) initially placed at $y_c = -0.15$ inside the channel subjected to electric field. (a) Profile of the rotating drop for $t^* = 0$ to 5.6. (b) The vector field in and around the drop for $t^* = 1.2,2.3,3.3$, 4.3, 15, and 20. (c) The trajectory of a marker point (marked as red dot) near the interface ($x^* = 1$, $y^* = 0.025$). The other parameters are Ca = 0.7, $\lambda = 1$, $E = 5$, $S = 2$, and $R = 0.5$. The flow field is presented in the frame of reference of the drop.

the higher shear stress tends to drift the droplet towards the channel center line. The combined effect of these results in the rotation of the droplet, which is further aided by the oblate shape of the drop. As the drop rotates, the influence of Magnus lift also comes into picture. It is to be noted that the present study is carried out for low Reynolds number flows inside a microchannel, wherein the influence of inertia is negligible. The lift force associated with the Magnus effect is dependent on the magnitude of both the translational as well as rotational velocity of the droplet. Due to the low migration velocity of the drop, the lift force generated is not significant in the face of a strong opposing effect of the applied electric force. The drops thus settle at a certain equilibrium position that is between the channel center line and initial off-center position. However, for the drops with lower permittivity ratio and higher conductivity ratio ($S < 1$ and $R > 1$), the elongation monotonically increases perpendicular to the flow direction, and the deformation is more pronounced at higher magnitude of the applied electric field.

Figure 18(a) shows the rotation of a drop inside the channel along with translation for $E = 5$ over a duration of time between $t^* = 0$ and $t^* = 5.6$. However, this phenomenon is prominently exhibited until $t^* = 15$ and gradually dampens out with time. The vector fields are illustrated in Fig. 18(b) for $t^* = 1.2,2.3,3.3$, 4.3, 15.0, and 30.0. Figure 18(c) depicts the trajectory of a marker point near the interface of the drop and the channel liquid ($x = 1, y = 0.025$). The position of the marker point (in red dot) inside the drop is shown for different time instants as the drop migrates inside the channel. The x coordinate depicts the translational displacement of the drop together with the comoving marker point, whereas the displacement in the y direction illustrates the effect of rotational (clockwise) motion of the marker point while the drop is in translational motion.

IV. CONCLUSIONS

In the present work, numerical simulations of a neutrally buoyant droplet migrating in a 2D channel in the creeping flow regime are performed using GERRIS. The Navier-Stokes equations coupled with electric force terms and continuity equations are solved to study droplet dynamics in a channel with fully developed flow at the inlet, with and without the influence of an electric field. Validations for the numerical solution are presented before proceeding with a detailed parametric study. The results obtained from the investigation are summarized in this section.

For a drop traversing in a Poiseuille flow at a very low Reynolds number, the effects of the initial position of the drop, drop size, capillary number, and viscosity ratio on its motion and deformation are thoroughly studied. It is observed that when a drop of size $a^* = 0.6$ is placed at different initial positions in the flow field for Ca = 0.7 and $\lambda = 1.0$, the drop gradually migrates towards the center line of the channel and eventually takes a steady lateral position. The initial y_c position was varied between -0.15 and 0.15. To understand the effect of drop size on cross-stream migration, we considered drops of sizes varying from $a^* = 0.3$ to 0.65 for the same flow condition (Ca = 0.7 and $\lambda = 1.0$). For the drops that are released from an initial off-center position, $y_c = -0.15$, it is observed that larger drops move more slowly in the channel as compared to smaller drops, but the lateral migration phenomenon is better exhibited by the larger drops. Drops of size $a^* = 0.3$ and 0.4 exhibit very little cross-migration phenomenon. From these studies (effect of initial position and size of the droplet), it is evident that the migration phenomenon of moderate size drops is quite interesting. Therefore, for the rest of the investigations the drop size is fixed at $a^* = 0.4$, and the initial off-center position is fixed at $y_c = -0.15$. An attempt has been made to understand the factors that enhance cross-stream migration. The effect of the capillary number on drop migration is studied by considering a drop of size of $a^* = 0.4$ placed at $y_c = -0.15$ for $\lambda = 1$. The capillary number is varied between Ca = 0.3 and 1.3, and it is observed that with the increase in Ca the drop migration increases. The effect of viscosity ratio on the drop migration is studied by varying λ between 0.01 and 2.5. This study concluded that with the increase in viscosity ratio the drop migration decreases.

In order to understand drop migration in a Poiseuille flow under the influence of an external electric field, we considered a drop of size, $a^* = 0.4$ placed at $y_c = -0.15$ for Ca = 0.7 and $\lambda = 1$. Both dielectric and leaky dielectric fluids are taken into consideration in this study. In the case of dielectric fluids, the effects of permittivity ratio (S) and the strength of electric field (E) on drop migration are studied. It is observed that for a drop fluid having high permittivity compared to the suspending

fluid, the drop deforms highly and oscillates around its mean position. When the electric field strength is increased from $E = 5$ to 20 for a fixed permittivity ratio, it is observed that the cross-stream migration increases and the drops become stretched and elongated in the direction of the electric field. In the case of leaky dielectric fluids, the electric field strength is varied from $E = 1$ to 5 and two sets of fluid combinations are considered. In one case the permittivity of the drop fluid is less than that of the suspending medium while the drop fluid is more conducting than the suspending fluid ($S = 0.5$ and $R = 2$), and in the other case, the conditions are reversed ($S = 2$ and $R = 0.5$). It is observed that a more conducting drop tends to migrate towards the channel center line and the cross migration increases with the increase in E, while a less conducting drop tends to settle down at a lateral position somewhere near the initial off-center position. An interesting phenomenon is revealed in the case of less conducting drops under a stronger electric field wherein the drops exhibit rotation together with translation.

ACKNOWLEDGMENT

G.B. acknowledges indebtedness to the J. C. Bose National Fellowship of DST, Government of India.

[1] H. Goldsmith and S. Mason, Nature (London) **190**, 1095 (1961).
[2] W. L. Olbricht, Annu. Rev. Fluid Mech. **28**, 187 (1996).
[3] B. P. Ho and L. G. Leal, J. Fluid Mech. **65**, 365 (1974).
[4] W. L. Olbricht and D. M. Kung, Phys. Fluids A **4**, 1347 (1992).
[5] P. C. H. Chan and L. G. Leal, J. Fluid Mech. **92**, 131 (1979).
[6] A. Nadim and H. A. Stone, Stud. Appl. Math. **85**, 53 (1991).
[7] H. Zhou and C. Pozrikidis, Phys. Fluids **6**, 80 (1994).
[8] M. J. Martinez and K. S. Udell, J. Fluid Mech. **210**, 565 (1990).
[9] T. M. Tsai and M. J. Miksis, J. Fluid Mech. **274**, 197 (1994).
[10] C. Coulliette and C. Pozrikidis, J. Fluid Mech. **358**, 1 (1998).
[11] A. J. Griggs, A. Z. Zinchenko, and R. H. Davis, Int. J. Multiphase Flow **33**, 182 (2007).
[12] Y. Wang and P. Dimitrakopoulos, Theor. Comp. Fluid Dyn. **26**, 361 (2012).
[13] S. Mortazavi and G. Tryggvason, J. Fluid Mech. **411**, 325 (2000).
[14] H. Konda, M. K. Tripathi, and K. C. Sahu, J. Fluid Eng. **138**, 064501 (2016).
[15] A. Nourbakhsh and S. Mortazavi, Iranian J. Sci. Technol. **34**, 179 (2010).
[16] B. Nath, G. Biswas, A. Dalal, and K. C. Sahu, Phys. Rev. E **95**, 033110 (2017).
[17] M. P. Borthakur, G. Biswas, and D. Bandyopadhyay, Phys. Rev. E **96**, 013115 (2017).
[18] C. T. O'Konski and H. C. Thacher, Jr., J. Phys. Chem. **57**, 955 (1953).
[19] C. Garton and Z. Krasucki, Proc. Royal Soc. Lond. A **280**, 211 (1964).
[20] G. Taylor, Proc. Royal Soc. Lond. A **291**, 159 (1966).
[21] O. O. Ajayi, Proc. Royal Soc. Lond. A **364**, 499 (1978).
[22] R. Allan and S. Mason, Proc. Royal Soc. Lond. A **267**, 45 (1962).
[23] T. Tsukada, T. Katayama, Y. Ito, and M. Hozawa, J. Chem. Eng. Jpn. **26**, 698 (1993).
[24] J. Q. Feng and T. C. Scott, J. Fluid Mech. **311**, 289 (1996).
[25] J. Baygents, N. Rivette, and H. Stone, J. Fluid Mech. **368**, 359 (1998).
[26] J. Berry, M. Davidson, and D. Harvie, J. Comput. Phys. **251**, 209 (2013).
[27] E. Lac and G. Homsy, J. Fluid Mech. **590**, 239 (2007).
[28] A. Fernández, G. Tryggvason, J. Che, and S. L. Ceccio, Phys. Fluids **17**, 093302 (2005).
[29] A. Fernández, Phys. Fluids **20**, 043304 (2008).
[30] A. Fernández, Phys. Fluids **20**, 043303 (2008).
[31] J. Hua, L. K. Lim, and C.-H. Wang, Phys. Fluids **20**, 113302 (2008).
[32] J. Zhang and D. Y. Kwok, J. Comput. Phys. **206**, 150 (2005).
[33] H. Sato, N. Kaji, T. Mochizuki, and Y. H. Mori, Phys. Fluids **18**, 127101 (2006).
[34] S. Timung, J. Chaudhuri, M. P. Borthakur, T. K. Mandal, G. Biswas, and D. Bandyopadhyay, Electrophoresis **38**, 1450 (2017).
[35] J. Brackbill, D. Kothe, and C. Zemach, J. Comput. Phys. **100**, 335 (1992).
[36] M. P. Borthakur, G. Biswas, and D. Bandyopadhyay, Phys. Rev. E **97**, 043112 (2018).
[37] S. Popinet, J. Comput. Phys. **190**, 572 (2003).
[38] S. Popinet, J. Comput. Phys. **228**, 5838 (2009).
[39] Y. Ling, J.-M. Fullana, S. Popinet, and C. Josserand, Phys. Fluids **28**, 062001 (2016).
[40] X. Chen, C. Xue, L. Zhang, G. Hu, X. Jiang, and J. Sun, Phys. Fluids **26**, 112003 (2014).
[41] M. K. Tripathi, K. C. Sahu, and R. Govindarajan, Nat. Commun. **6**, 6268 (2015).
[42] J. López-Herrera, S. Popinet, and M. Herrada, J. Comput. Phys. **230**, 1939 (2011).
[43] C. Ferrera, J. López-Herrera, M. Herrada, J. Montanero, and A. Acero, Phys. Fluids **25**, 012104 (2013).
[44] R. Cimpeanu, D. T. Papageorgiou, and P. G. Petropoulos, Phys. Fluids **26**, 022105 (2014).
[45] C. Burcham and D. Saville, J. Fluid Mech. **405**, 37 (2000).
[46] S. Maehlmann and D. T. Papageorgiou, J. Fluid Mech. **626**, 367 (2009).
[47] A. Karimi, S. Yazdi, and A. M. Ardekani, Biomicrofluidics **7**, 021501 (2013).